RSC Advances

PAPER

View Article Online
View Journal | View Issue

Cite this: *RSC Adv.*, 2024, **14**, 35505

Design, synthesis, and evaluation of novel thiadiazole derivatives as potent VEGFR-2 inhibitors: a comprehensive *in vitro* and *in silico* study†

Ibrahim H. Eissa, *[a] Walid E. Elgammal, [b] Hazem A. Mahdy, [a] Susi Zara,[c] Simone Carradori, [c] Dalal Z. Husein,[d] Maymounah N. Alharthi, [e] Ibrahim M. Ibrahim,[f] Eslam B. Elkaeed,*[g] Hazem Elkady [a] and Ahmed M. Metwaly *[h]

Objective: This study aims to investigate the potential of designed 2,3-dihydro-1,3,4-thiadiazole derivatives as anti-proliferative agents targeting VEGFR-2, utilizing a multidimensional approach combining *in vitro* and *in silico* analyses. Methods: The synthesized derivatives were evaluated for their inhibitory effects on MCF-7 and HepG2 cancer cell lines. Additionally, VEGFR-2 inhibition was assessed. Further investigations into the cellular mechanisms were conducted to elucidate the effects of **20b** (*N*-(4-((*E*)-1-(((*Z*)-5-Acetyl-3-(*p*-tolyl)-1,3,4-thiadiazol-2(3*H*)-ylidene)hydrazono) ethyl) phenyl) benzamide) on cell cycle arrest and apoptosis induction. Furthermore, computational investigations, including molecular docking, MD simulations, DFT calculations, MM-GBSA, PCAT, and ADMET predictions were conducted. Results: Compound **20b** emerged as a standout candidate with significantly lower IC_{50} values of 0.05 μM and 0.14 μM for MCF-7 and HepG2 cell lines, respectively. It exhibited notable VEGFR-2 inhibition (0.024 μM), surpassing the efficacy of sorafenib (0.041 μM). Compound **20b** demonstrated cancer-specific targeting potential with a high selectivity index in normal WI-38 cells (IC_{50} 0.19 μM). Mechanistic studies revealed its ability to arrest the cell cycle of MCF-7 cells and induce apoptosis (total apoptosis 34.47%, early apoptosis 18.48%, and late apoptosis 15.99%), supported by upregulated caspase-8 (3.42-fold) and caspase-9 (5.44-fold) expression. Additionally, **20b** arrested the cell cycle of MCF-7 cells at the %G0-G1 phase. Computational investigations provided insights into its molecular interactions with VEGFR-2, contributing to the rational design and understanding of its pharmacological profile. Conclusions: Compound **20b** presents as a promising anti-proliferative agent targeting VEGFR-2. Also, this comprehensive investigation underscores the potential of 2,3-dihydro-1,3,4-thiadiazole derivatives as promising candidates for further development in anti-cancer research.

Received 6th June 2024
Accepted 25th October 2024

DOI: 10.1039/d4ra04158e

rsc.li/rsc-advances

1. Introduction

The number of new cancer cases is anticipated to exceed 35 million by 2050, representing a 77% rise from the estimated 20 million cases in 2022.[1] These statistics highlight the substantial worldwide impact of cancer, emphasizing the necessity for ongoing and extensive scientific research to create innovative treatment methods. Angiogenesis, involving Vascular Endothelial Growth Factor (VEGF) and its receptor VEGFR-2, is pivotal in the development of both cancer and cardiovascular diseases.[2,3] VEGFR-2 functions include promoting vessel development and regulating the proliferation, migration, and survival of endothelial cells in vasculogenesis and angiogenesis.[4] Ongoing research has identified a significant correlation between increased VEGFR-2 expression and resistance of the anti-cancer drugs, heightened angiogenesis, and reduced

[a]*Department of Pharmaceutical Medicinal Chemistry & Drug Design, Faculty of Pharmacy (Boys), Al-Azhar University, Cairo, 11884, Egypt. E-mail: Ibrahimeissa@azhar.edu.eg*

[b]*Chemistry Department, Faculty of Science, Al-Azhar University, Nasr City, Cairo 11751, Egypt*

[c]*Department of Pharmacy, "G. d'Annunzio" University of Chieti-Pescara, Chieti, 66100, Italy*

[d]*Department of Chemistry, Faculty of Science, New Valley University, El-Kharja 72511, Egypt*

[e]*Department of Chemistry, College of Science, Princess Nourah bint Abdulrahman University, P.O. Box 84428, Riyadh 11671, Saudi Arabia*

[f]*Department of Biophysics, Faculty of Science, Cairo University, Giza 12613, Egypt*

[g]*Department of Pharmaceutical Sciences, College of Pharmacy, AlMaarefa University, P.O. Box 71666, Riyadh 11597, Saudi Arabia. E-mail: ekaeed@um.edu.sa*

[h]*Department of Pharmacognosy and Medicinal Plants, Faculty of Pharmacy (Boys), Al-Azhar University, Cairo 11884, Egypt. E-mail: ametwaly@azhar.edu.eg*

† Electronic supplementary information (ESI) available. See DOI: https://doi.org/10.1039/d4ra04158e

apoptosis.[5] Accordingly, targeting VEGFR-2 has been introduced as a promising therapeutic approach.[6] Anti-VEGFR-2 drugs are designed to inhibit VEGFR-2, a receptor tyrosine kinase crucial for angiogenesis in tumor cells.[7,8] While these inhibitors effectively treat various cancers, they often come with serious side effects, including hypertension, nephropathy,[9] proteinuria,[10] cardiac ischemia,[11] reversible posterior leukoencephalopathy syndrome,[12] and potential links to germline polymorphisms.[13] Consequently, the development of new anti-VEGFR-2 candidates holds potential to enhance treatment efficacy, patient's health, and advance the standard of cancer care.

The integrated approach, combining computational (*in silico*) and experimental (*in vitro*) methods, serves to validate the efficacy of active anticancer compounds while laying the groundwork for future enhancements and practical applications.[14] This harmonious blend of approaches not only affirms the compounds' effectiveness in laboratory settings but also guides the refinement and optimization of their design.[15] The insights gained from this integrated strategy hold the potential of targeted cancer therapies, emphasizing the promise of new derivatives as a notable class of compounds with substantial anticancer activity.[16] In essence, the study's combination of experimental and computational methods advances these findings towards practical applications, offering hope for the development of more effective anticancer treatments.

Our research teamwork has previously discovered a variety of potential anti-VEGFR-2 compounds exhibiting anticancer properties including quinolones,[17] isatins,[18] nicotinamides,[19,20] thiazolidines,[21] pyridines,[22] theobromines,[23–27] naphthalenes,[28] and indoles.[29] Thiadiazole derivatives have gained recognition in medicinal chemistry due to their diverse pharmacological actions, including anticancer and anti-inflammatory properties.[30–33]

This study introduces new 2,3-dihydro-1,3,4-thiadiazole derivatives, with a specific focus on compound **20b**, identified as a potent VEGFR-2 inhibitor through molecular docking studies.

1.1 Rationale

Many drugs have been approved by the FDA-approved as VEGFR-2 inhibitors for the treatment of several types of cancers.[34] Sorafenib **I**,[35] lenvatinib **II**,[36] sunitinib **III**,[37] and toceranib **IV** (ref. 38) are well-known examples of FDA-approved VEGFR-2 inhibitors (Fig. 1). VEGFR-2 inhibitors are characterized by four essential pharmacophoric features crucial for effective binding with the ATP binding site of VEGFR-2. These features are as follows: (i) a hetero-aromatic system: This component is designed to occupy the hinge region, ensuring a specific arrangement within the molecular structure for optimal interaction;[39] (ii) a linker moiety: Positioned to orient into the region between the DFG domain and the hinge region, this linker serves as a critical element facilitating the proper spatial alignment of the inhibitor within the active site.;[40] (iii) a pharmacophore moiety: Comprising at least one H-bond donor and one H-bond acceptor group, this pharmacophore is strategically positioned to occupy the DFG domain. It plays a pivotal role in establishing hydrogen bond interactions, enhancing the inhibitor's affinity for the target;[41] (iv) a terminal hydrophobic moiety: Positioned to occupy the allosteric hydrophobic pocket of the ATP binding site, this terminal hydrophobic component contributes to the overall stability and specificity of the inhibitor's binding[42–44] (Fig. 1).

Depending on the ligand-based drug design approach, a new series of 2,3-dihydro-1,3,4-thiadiazole derivatives was designed as VEGFR-2 inhibitors. The designed compounds involve 2,3-dihydro-1,3,4-thiadiazole moiety as a hetero-aromatic system that can occupy the hinge region. In addition, the 1-phenylethylidenehydrazine moiety was utilized as a linker group. Furthermore, the amide group was utilized as a pharmacophore moiety to occupy the DFG domain. Finally, different substituted phenyl rings were used as hydrophobic tails of the designed molecules (Fig. 1).

2. Results and discussion

2.1. Chemistry

Schemes 1–3 describes the pathways that have been followed to synthesize the desired derivatives. At first, the starting intermediates **5a,b** and **8** were meticulously synthesized. This involved subjugating the 1,3-diketones (acetylacetone **1** and/or ethyl acetoacetate **6**) to a chlorination reaction using sulfuryl dichloride (SO_2Cl_2).[45] Subsequently, the resulting products (**2** and **7**, respectively) were allowed to react with the appropriate diazonium salts **4** of aromatic amines **3** to produce the key intermediates **5a,b** and **8**. The diazonium salts were obtained from the reaction of the substituted aromatic amines **3** with a solution of sodium nitrite in the presence of aqueous hydrochloric acid in an ice bath[46] (Scheme 1).

On the other hand, Scheme 2 illustrates the synthesis of compound **16**. The first step entailed synthesizing *N*-(4-acetylphenyl)acetamide **14**, as previously documented.[47] The accomplishment was made through the reaction of 4-aminoacetophenone **10** with acetic acid anhydride **13** as the acetylating agent in DMF utilizing trimethylamine (TEA) as a base. Afterward, compound **14** underwent reflux with methyl hydrazinecarbodithioate **12**,[48] in pure ethanol, synthesizing the desired compound **15**. This compound was then reacted with (*E*)-2-oxo-*N*-(*p*-tolyl)propanehydrazonoyl chloride **5b** in ethanol to produce the corresponding 2,3-dihydro-1,3,4-thiadiazoles derivative **16**.

Likewise, the benzoylation of 4-aminoacetophenone **10** using (un)substituted benzoyl chloride **17a,b** under identical acylation conditions resulted in the formation of the isolated products **18a,b**. Subsequently, compounds **18a,b** were condensed with methyl hydrazinecarbodithioate **12** in absolute ethanol to yield compounds **19a,b**, which were obtained in their pure form through recrystallization from a mixture of methanol and dichloromethane. Eventually, the hetrocyclization of compounds **19a,b** was achieved by the reaction with substituted hydrazonoyl chlorides **5a,b** and/or **8** in a heated solution of EtOH/TEA to give **20a,b** and **21a,b**, respectively.

2.2. Biology

2.2.1. Anti-proliferative effect. Table 1 illustrates the inhibitory concentration (IC_{50}) values, measured in micromolar

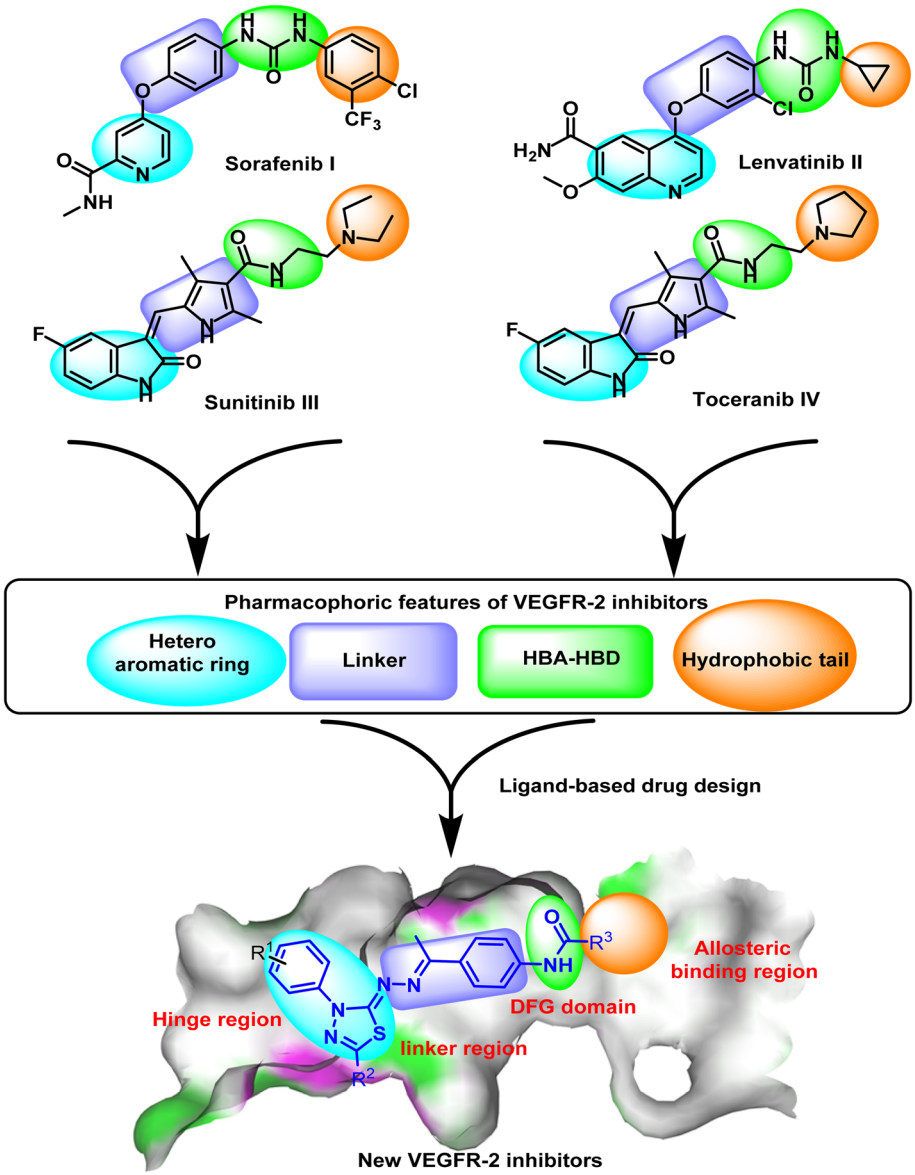

Fig. 1 Rationale of the molecular design.

concentration (μM), for the new thiadiazole derivatives on MCF-7 and HepG2 cancer cell lines. Notably, compound **20b** emerges as a highly potent inhibitor, demonstrating an IC_{50} value of 0.05 μM against MCF-7 and 0.14 μM against HepG2. This suggests a pronounced efficacy in restraining the growth of cancer cells, as lower IC_{50} values indicate heightened potency. Additionally, the consistently lower IC_{50} values observed across derivatives (**20a**, **20b**, **21a**, **21b**) in contrast to compound **16** imply a successful design strategy in enhancing the anti-proliferative potential of these compounds.

While the IC_{50} values provide valuable insights into the potency of the compounds, it is advisable to conduct additional studies to gain a more comprehensive understanding of their anti-proliferative efficacy. In conclusion, the presented IC_{50} values suggest that compound **20b** and its derivatives hold promise as potent anti-proliferative agents, warranting further investigation.

2.2.2. *In vitro* VEGFR-2 assay. Notably, compound **20b** demonstrates superior VEGFR-2 inhibition (0.024 ± 0.004 μg mL^{-1}) compared to sorafenib (0.041 ± 0.002 μg mL^{-1}), suggesting its effectiveness in hampering angiogenesis as presented in Table 2. This aligns with its robust anti-proliferative activity observed in MCF-7 and HepG2 cell lines, reinforcing the notion that **20b**'s efficacy is, in part, due to VEGFR-2 inhibition. The data positions compound **20b** as a promising candidate for further development in cancer therapeutics, particularly for tumors where VEGFR-2 signaling is crucial.

2.2.3. Kinase profiling test. The previous results encouraged us to test compound **20b** against other different kinases including CDK8, PIK3α, BRAF, and EGFR to reach a good insight about its kinases inhibitory profile and to confirm its selectivity against VEGFR-2. Cortistatin A, PIK-90, Vemurafenib, and Erlotinib were used as reference standards for CDK8, PIK3α, BRAF, and EGFR, respectively.

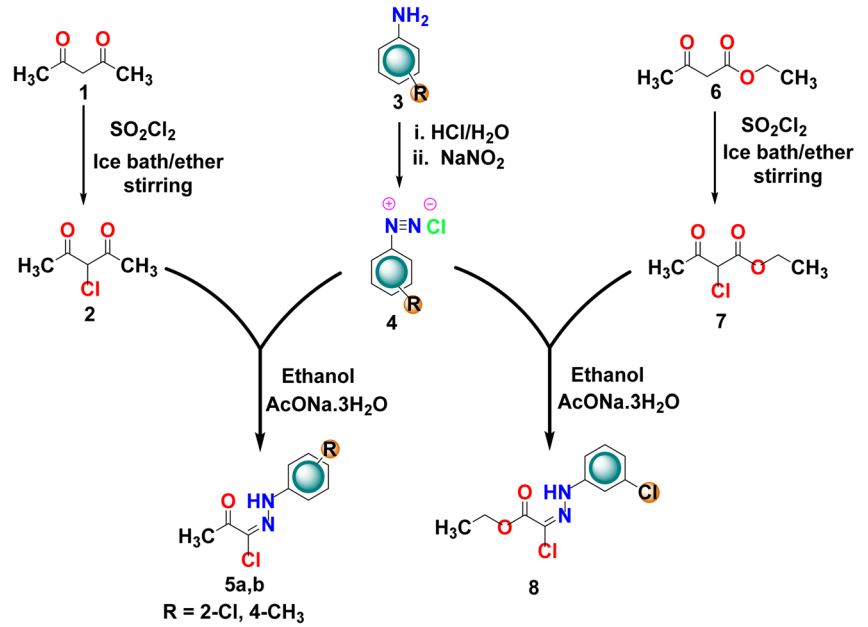

Scheme 1 Synthesis of key intermediates **5a,b** and **8**.

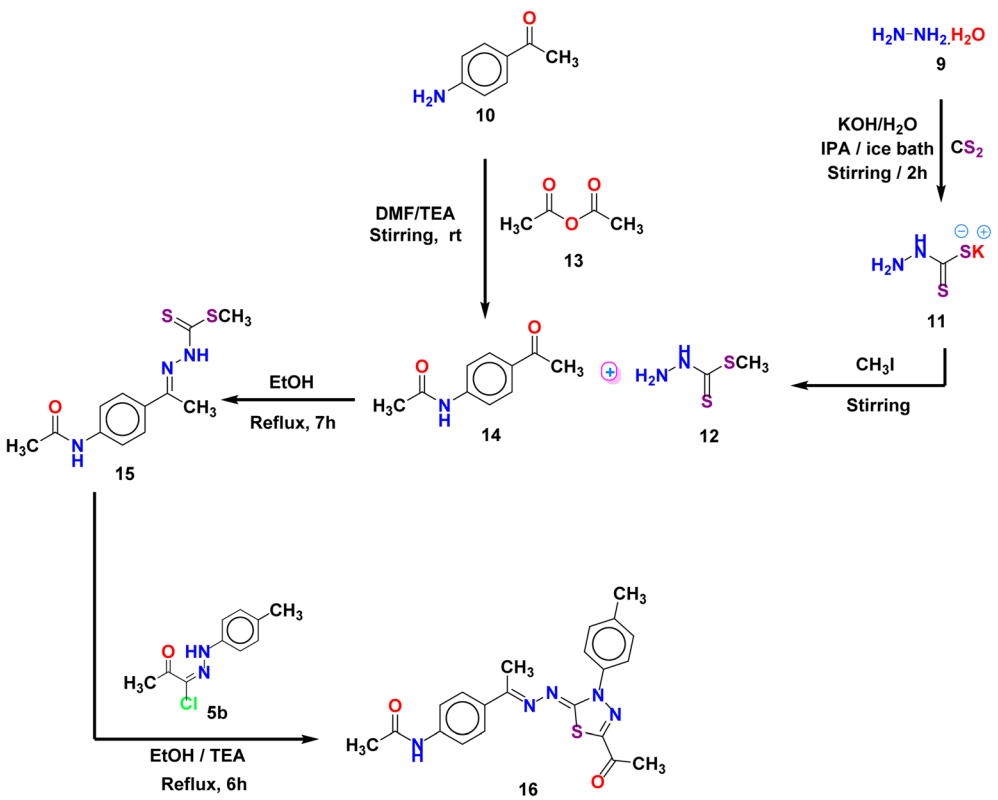

Scheme 2 A classical method for the synthesis of 2,3-dihydro-1,3,4-thiadiazole derivative **16**.

Results in Table 3 showed that compound **20b** showed moderate to weak inhibition values against the four investigated protein kinases in comparison to the selected reference kinase inhibitors. For its activity against CDK8, compound **20b** showed IC_{50} value of 0.266 ± 0.058 μM, compared to Cortistatin A (IC_{50} = 0.032 ± 0.004 μM). Regarding its activity against PIK3α, it showed IC_{50} value of 2.143 ± 0.095 in comparison to PIK-90 (IC_{50} = 2.143 ± 0.095 μM). Additionally, compound **20b** demonstrated weak inhibitory activities against BRAF (IC_{50} = 5.841 ± 0.250 μM) and EGFR (IC_{50} = 1.431 ± 0.085 μM)

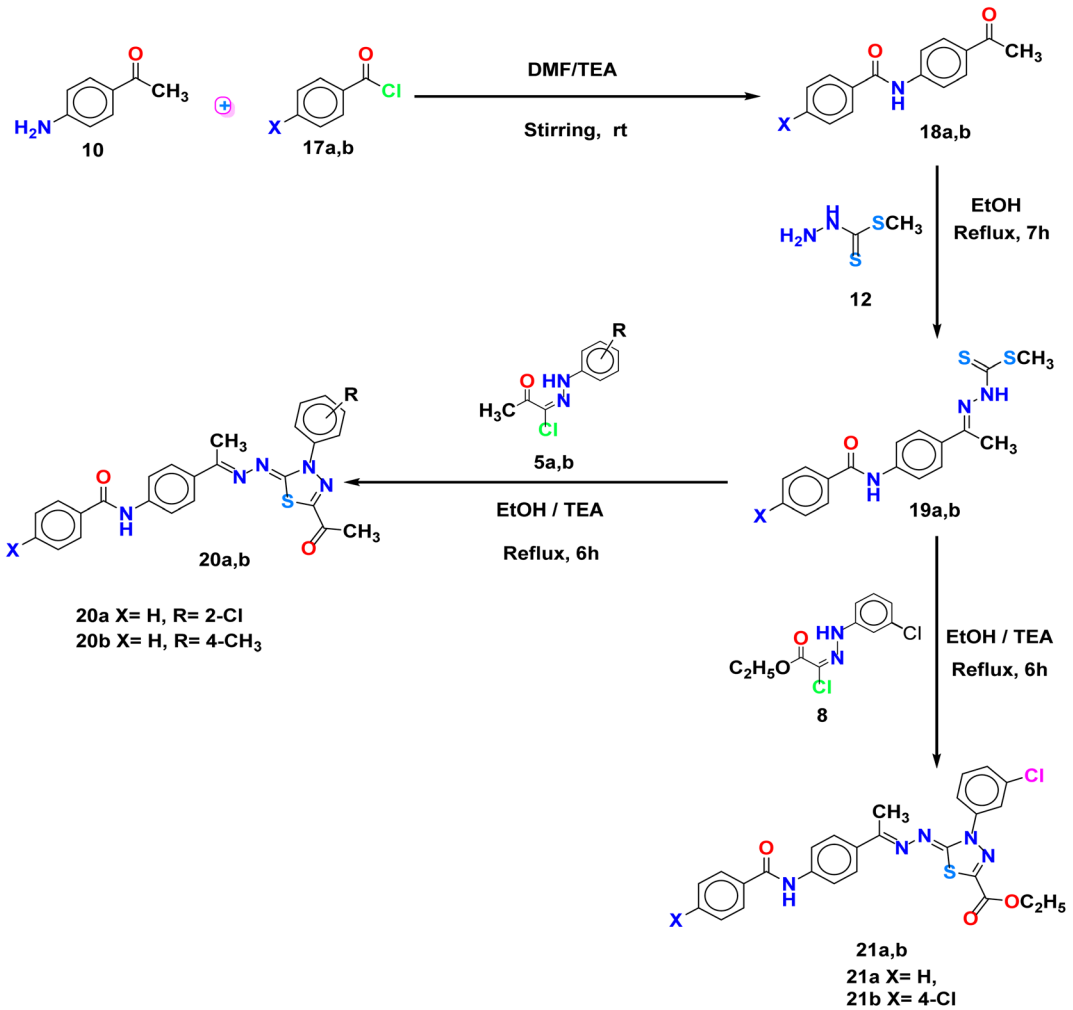

Scheme 3 A classical method for the synthesis of acetyl and ester of 2,3-dihydro-1,3,4-thiadiazole derivatives **20a,b** and **21a,b**.

Table 1 The anti-proliferative impact of **16**, **20a,b** and **21a,b** on the cell proliferation of MCF-7 and HepG2 cell lines

	MCF-7 (IC_{50})[a] (μM)	HepG2 (IC_{50})[a] (μM)
16	1.25 ± 0.02	9.92 ± 0.22
20a	0.06 ± 0.01	0.13 ± 0.01
20b	0.05 ± 0.01	0.14 ± 0.01
21a	0.19 ± 0.01	0.15 ± 0.01
21b	0.14 ± 0.01	0.13 ± 0.01
Sorafenib	0.14 ± 0.03	0.13 ± 0.03

[a] Data are mean of three different experiments' IC_{50} values.

Table 2 VEGFR-2 inhibitory activity of the most active compound, **20b**

Comp.	VEGFR-2 IC_{50}[a] (μg mL^{-1})	VEGFR-2 IC_{50}[a] (μM)
20b	0.024 ± 0.004	0.051 ± 0.004
Sorafenib	0.041 ± 0.002	0.088 ± 0.002

[a] Data are mean of three different experiments' IC_{50} values.

compared to those of Vemurafenib (IC_{50} = 0.347 ± 0.029 μM) and Erlotinib (IC_{50} = 0.005 ± 0.001 μM). From these results, we can found that compound **20b** has no selectivity against the tested four kinases but it has a great selectivity against VEGFR-2 receptor.

2.2.4. Safety and selectivity. The selectivity index (SI) provides a measure of a compound's preference for inhibiting cancer cell growth compared to normal cells. To calculate the SI of compound **20b**, its *in vitro* cytotoxicity against normal human lung cells (WI-38) was conducted and the formula: SI = IC_{50} in normal cells/IC_{50} in cancer cells was applied. Regarding compound **20b**, as shown in Table 4, the IC_{50} value in normal WI-38 cells is 0.19 μM. Accordingly, **20b**'s selectivity for MCF-7: SI = 0.19 μM/0.05 μM = 3.8 and for HepG2: SI = 0.19 μM/0.14 μM = 1.4. The calculated high SI values indicate a potential selectivity for MCF-7 over normal cells. These values suggest that compound **20b** exhibits a higher inhibitory effect on the growth of MCF-7 cancer cells compared to normal WI-38 cells, as indicated by the SI value greater than 1. However, further investigations would be essential to validate and understand the activity profile comprehensively.

Table 3 IC_{50} values of the tested compounds as CDK8, PIK3α, BRAF & EGFR kinases inhibition assay

Comp.	CDK8 IC_{50} (μM) (mean ± SD)	PIK3α IC_{50} (μM) (mean ± SD)	BRAF IC_{50} (μM) (mean ± SD)	EGFR IC_{50} (μM) (mean ± SD)
20b	0.266 ± 0.058	2.143 ± 0.095	5.841 ± 0.250	1.431 ± 0.085
Cortistatin A	0.032 ± 0.004	—	—	—
PIK-90	—	0.033 ± 0.008	—	—
Vemurafenib	—	—	0.347 ± 0.029	—
Erlotinib	—	—	—	0.005 ± 0.001

Table 4 The anti-proliferative impact of compound **20b** on the cell proliferation of WI-38 cell lines and its selectivity

Comp.	WI-38 IC_{50}[a] (μM)	Selectivity index	
		MCF-7	HepG2
20b	0.19 ± 0.01	3.8	1.4

[a] Data are mean of three different experiments' IC_{50} values.

2.2.5. Cellular mechanistic studies

2.2.5.1 Cell cycle analysis. The cell cycle distribution percentages for MCF-7 cells treated with compound **20b** and untreated MCF-7 cells were conducted by flow cytometry and were presented in Table 5 and Fig S1.† The cell cycle distribution analysis reveals notable alterations induced by compound **20b** in MCF-7 cells. Specifically, there is an increase in the percentage of cells in the G0–G1 phase from 62.37% (untreated MCF-7) to 69.25% (compound **20b**). This suggests that compound **20b** may impede cell cycle progression by inducing cell cycle arrest at the G0–G1 phase. Concomitantly, there is a decrease in the percentage of cells in the S phase from 23.91% (untreated MCF-7) to 18.76% (compound **20b**), indicating a potential reduction in DNA synthesis. Moreover, there is a slight decrease in the G2/M phase to be 11.99% (compound **20b**) instead of 13.72% (untreated MCF-7), suggesting a modest impact on the transition to mitosis. These changes in cell cycle distribution are indicative of the regulatory effects of compound **20b** on the cell cycle dynamics of MCF-7 cells. The observed arrest at the G0–G1 phase suggests that the compound may interfere with key checkpoints, preventing cells from progressing into the synthesis and mitotic phases. Such cell cycle modulation is a crucial aspect of anti-proliferative mechanisms, as disruption of cell cycle progression can lead to reduced cell proliferation and increased susceptibility to apoptosis.

Table 5 Impact of compound **20b** on the cell cycle progression of MCF-7 cells

Sample	Cell cycle distribution (%)		
	% G0-G1	% S	% G2/M
20b	69.25	18.76	11.99
Control	62.37	23.91	13.72

The findings underscore the potential of compound **20b** as a cell cycle regulator in MCF-7 cells, demonstrating its ability to influence the delicate balance of cell cycle phases. Overall, the observed alterations in cell cycle distribution suggest that compound **20b** holds promise as a candidate for further exploration in the development of targeted therapies against cancer cells.

2.2.5.2 Apoptosis assay. The flow cytometry assay was performed to evaluate the apoptosis analysis in MCF-7 cells, comparing untreated MCF-7 cells to those treated with compound **20b**. The apoptosis analysis (Table 6 and Fig. S2†) reveals a remarkable difference in the percentage of apoptotic cells between untreated MCF-7 cells and those treated with compound **20b**. Specifically, total apoptosis after treatment with compound **20b** is substantially higher at 34.47% compared to 0.85% in the untreated cells. This increase is indicative of the promising pro-apoptotic effect exerted by compound **20b**.

Breaking down the stages of apoptosis, the early apoptosis percentage increases from 0.61% in the untreated MCF-7 cells to a notable 18.48% after treatment. Concurrently, the percentage of cells in late apoptosis rises from 0.24% to 15.99%. These findings collectively suggest that compound **20b** induces both early and late apoptosis, indicating a multifaceted impact on the apoptotic pathways of MCF-7 cells. In contrast, the percentage of cells undergoing necrosis, a form of cell death associated with cellular damage, is relatively low but still increases from 1.43% in the untreated MCF-7 cells to 4.14% with compound **20b**. This suggests that compound **20b** may trigger a modest degree of necrosis in addition to its pronounced apoptotic effects.

The substantial increase in apoptosis, particularly in the early and late stages, highlights the potent cytotoxic effects of compound **20b** on the MCF-7 cells. Apoptosis is a fundamental process that eliminates damaged or abnormal cells, and the observed increase suggests that compound **20b** may have significant potential as an inducer of programmed cell death in cancer cells. These findings underscore the importance of apoptosis induction as a key mechanism in the anti-

Table 6 The influence of compound **20b** on different stages of cell death in MCF-7 cells

	Total	Early apoptosis	Late apoptosis	Necrosis
Compound **20b**	38.55	18.48	15.99	4.14
Control	2.28	0.61	0.24	1.43

Table 7 Caspase-8 and caspase-9 expression after compound **20b** treatment using RT-PCR analysis

	RT-PCR (fold change)	
	Caspase-8	Caspase-9
Compound **20b**	3.4176	5.4353
Control	1	1

proliferative activity of compound **20b** and position it as a promising candidate for further exploration in anti-cancer drug discovery.

2.2.5.3 Reverse transcription polymerase chain reaction (RT-PCR) studies. Table 7 presents the results of the RT-PCR analysis, indicating the fold change in the expression levels of caspase-8 and caspase-9 in MCF-7 cells treated with compound **20b** compared to untreated control. In detail, the RT-PCR results demonstrate a substantial increase in the expression levels of both caspase-8 and caspase-9 in MCF-7 cells treated with compound **20b** compared to the untreated control. The fold change for caspase-8 is 3.4176, indicating a more than 3-fold increase, while caspase-9 shows an even higher fold change of 5.4353.

Caspase-8 and caspase-9 are integral components of the apoptotic pathway, playing crucial roles in initiating and executing programmed cell death. The upregulation of these caspases in response to compound **20b** treatment confirms a pronounced activation of apoptotic pathways in MCF-7 cells. This alignment between apoptotic marker upregulation and increased apoptosis supports the notion that compound **20b** exerts its anti-proliferative effects through the induction of apoptosis in MCF-7 cells. Apoptosis induction, especially through the activation of key caspases, is a crucial mechanism in eliminating cancer cells. The specific targeting of apoptotic pathways aligns with the compound's overall impact on cell cycle distribution and apoptosis percentages, providing a coherent picture of its anti-proliferative properties.

2.3. Molecular docking study

MOE (Molecular Operating Environment, version 2019) software was utilized to conduct molecular docking simulations to explore potential drug binding patterns within the active site of VEGFR-2. The docking calculations employed the crystal structure of VEGFR-2 (PDB ID: 2OH4), with sorafenib, a known effective drug, serving as the reference compound.

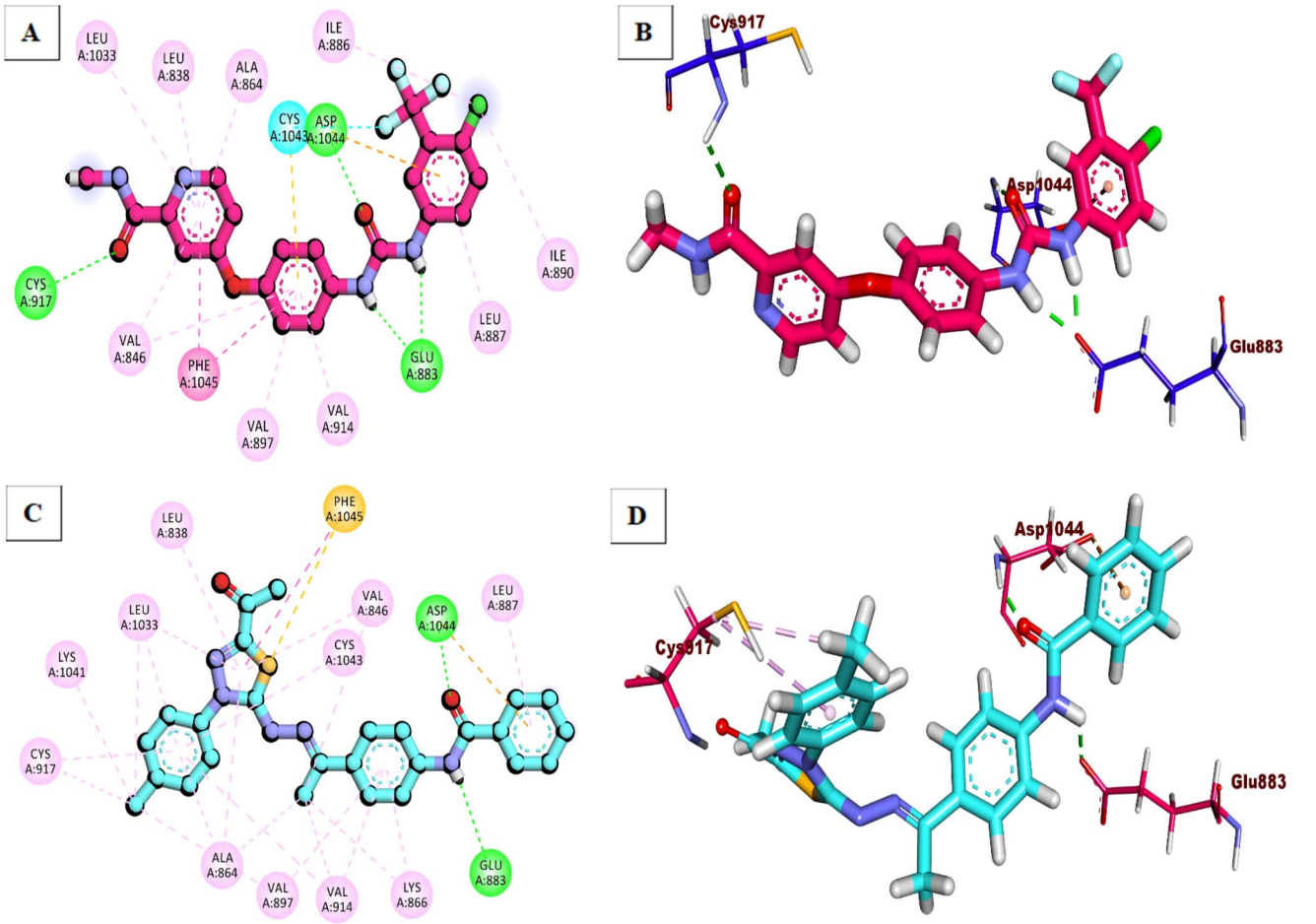

Fig. 2 Binding of the tested compounds against VEGFR-2. (A) 2D of sorafenib, (B) 3D of sorafenib, (C) 2D of compound **20b** and (D) 3D of compound **20b**.

In this section, we chose compound **20b** as the template control for the docking investigation since it has the strongest anti-proliferative activity against the tested cell lines. According to Fig. 2, compound **20b** was discovered to have been inserted into the deep cleft of the ATP binding site in the hinge region forming stable hydrophobic bonds with Cys917. The terminal amide also enabled the insertion of compound **20b** into the DFG motif region by forming two crucial hydrogen bonds between Glu883 and Asp 1044 at distances of 2.16 and 1.88, respectively.

2.4. MD simulation

During the simulation (200 ns), the root-mean-square deviation (RMSD) values for the reference system (VEGFR-2_sorafenib) exhibited stability, maintaining a consistent value of approximately 2.5 Å (indicated by the red line). In contrast, the RMSD

Fig. 3 The molecular dynamics simulation results for the VEGFR-2_**20b** complex, featuring (A) RMSD values for VEGFR-2, (B) RMSD values for the ligands, (C) radius of gyration, (D) solvent-accessible surface area (SASA), (E) changes in hydrogen bonds, (F) RMSF for the VEGFR-2 protein, and (G) distance from the center of mass. The red line represents the VEGFR-2_sorafenib complex, while the dark green line represents the VEGFR-2_**20b** complex.

values for the VEGFR-2_**20b** system (represented by the dark green line) initially showed an upward trend during the first 120 ns of the simulation. After this period, the values stabilized at around 4.2 Å (Fig. 3A). For the compound **20b** alone (dark green line), the RMSD showed a slight increasing trend in the initial 100 ns before reaching a stable value of approximately 2.9 Å (Fig. 3B). On the other side, sorafenib (red line) showed a more stable profile throughout the simulation, with an average RMSD of about 1.5 Å, indicating stronger binding stability. Furthermore, Fig. 3C illustrates a subtle difference in the radius of gyration's average (RoG) between the two systems. The VEGFR-2_sorafenib system had a lower RoG value of around 20.4 Å, compared to the VEGFR-2_**20b** system, which had an RoG of approximately 20.9 Å. This suggests that the protein-ligand complex with sorafenib is slightly more compact than with compound **20b**. Additionally, as shown in Fig. 3D, both systems exhibited similar average solvent-accessible surface area (SASA) values, each around 17 500 $Å^2$, indicating comparable exposure of the protein surfaces to the solvent. Fig. 3E provides insights into the hydrogen bonding patterns during the simulation. Compound **20b** consistently maintained nearly a hydrogen bond throughout the 200 ns of the simulation duration, whereas sorafenib fluctuated between forming one and two hydrogen bonds. In terms of structural stability, the root-mean-square fluctuation (RMSF) profiles revealed that both systems maintained overall structural integrity with minimal deviations. The primary difference was observed in the oscillations of the C-alpha atoms within the Ile1042 loop. In the reference system (VEGFR-2_sorafenib), the RMSF reached a maximum of 6 Å, whereas in the VEGFR-2_**20b** system, it increased to about 8 Å (Fig. 3F), indicating slightly greater flexibility in the latter. Additionally, the average distance between the protein's center of mass and the ligand was stable in both systems. For compound **20b**, this distance was approximately 9.3 Å, suggesting a stable interaction, though it was slightly greater than the reference compound, sorafenib, by about 1.5 Å (Fig. 3G). This difference in distance further highlights the slightly more stable binding conformation of sorafenib within the active site of VEGFR-2. Overall, these results show that both VEGFR-2-ligand complexes remained stable structurally, with minor differences in dynamic behavior and interaction patterns.

Fig. 4 illustrates the various components of the predicted binding free energy, calculated using the MM-GBSA method. The binding energy for molecule **20b** is −3.9 kcal mol^{-1}, in contrast to sorafenib's average of −43.3 kcal mol^{-1}, indicating significant differences in the components influencing binding. The van der Waals bondings are almost identical for both systems, averaging around −50 kcal mol^{-1}. However, electrostatic interactions are more favorable for sorafenib compared to **20b** (−17.92 kcal mol^{-1} *versus* +0.91 kcal mol^{-1}). This contributes to the lower total binding energy of **20b** relative to the reference compound. Additionally, the solvation energy (Egb) for **20b** is less favorable than for sorafenib.

To determine the contribution of each amino acid within 1 nm of each ligand, a decomposition analysis was performed (Fig. 5). Six amino acids showed a more significant share to the binding affinity of **20b** compared to sorafenib:

Leu838: 1.65 kcal mol^{-1} (**20b**) *versus* 1.13 kcal mol^{-1} (sorafenib).

Val846: −1.58 kcal mol^{-1} (**20b**) *versus* 1.2 kcal mol^{-1} (sorafenib).

Val897: −1.31 kcal mol^{-1} (**20b**) *versus* −0.96 kcal mol^{-1} (sorafenib).

Val914: −1.97 kcal mol^{-1} (**20b**) *versus* −1.14 kcal mol^{-1} (sorafenib).

Phe916: −1.08 kcal mol^{-1} (**20b**) *versus* −1.06 kcal mol^{-1} (sorafenib).

Asp1044: −1.46 kcal mol^{-1} (**20b**) *versus* −1.41 kcal mol^{-1} (sorafenib).

Phe1045: −2.17 kcal mol^{-1} (**20b**) *versus* −0.86 kcal mol^{-1} (sorafenib).

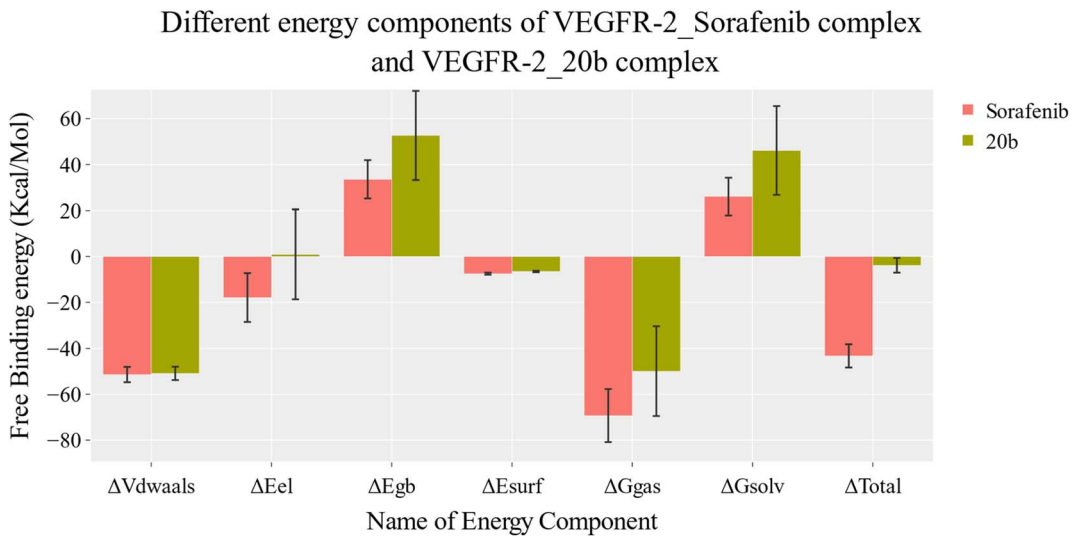

Fig. 4 The energetic components of the MM-GBSA method and their respective values for the two systems. The bars represent the standard deviations of these values.

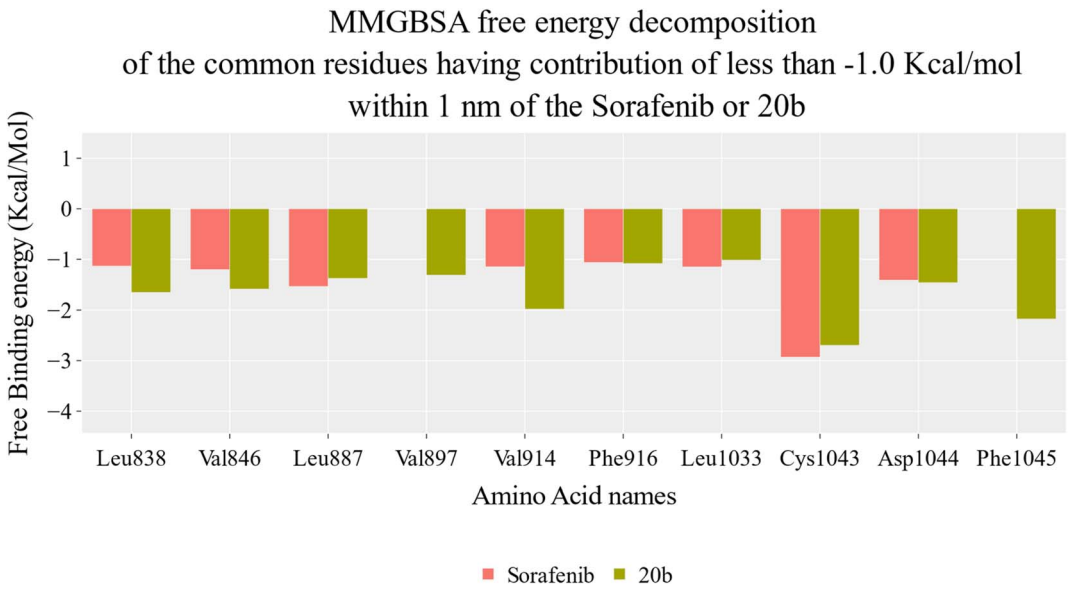

Fig. 5 A comparison between the decomposition of the binding free energy of the VEGFR-2_**20b** and VEGFR-2_sorafenib complexes. The highlighted amino acids are those found within 1 nm of each ligand, present in both complexes, and demonstrating a binding affinity of −1 kcal mol^{-1} or higher.

These values highlight the enhanced binding energy of compound **20b** with these specific amino acids compared to sorafenib, providing insights into the molecular interactions that contribute to the improved binding of **20b** in comparison to sorafenib.

To get more information about the Protein–Ligand Interaction Fingerprints (ProLIF) and Principal Component Analysis (PCA), see Fig. S3–S10.†

2.5. DFT studies

One of the most popular and reliable techniques for estimating molecular systems as well as their electronic characteristics is the DFT/B3LYP approach. The molecular system of compound **20b** is selected due to its remarkable reactivity as conducted practically. Using the Gaussian 09 package, the basis set 6-31G with double zeta plus polarization (d,p) was applied through the density functional theory (DFT/B3LYP) approach to optimize the molecular structure of **20b**. The chemical structure was plotted using Gauss View 05 and the optimized output file was analyzed using Multiwfn, GaussSum, and AIMAll programs. Based on the global reactivity parameters and band gap energy, the reactivity of the selected compound is predicted. The optimized geometry with atom numbering is presented in Fig. 6a. Compound **20b** is a polar molecule as its calculated dipole moment was found to be 7.257 Debye (Table 8), which indicates a higher tendency to interact with targets (amino acids). The high polarity of a given molecule increases the potential interatomic forces such as hydrogen bonding and dipole–dipole interactions between the selected molecule and the amino acids.

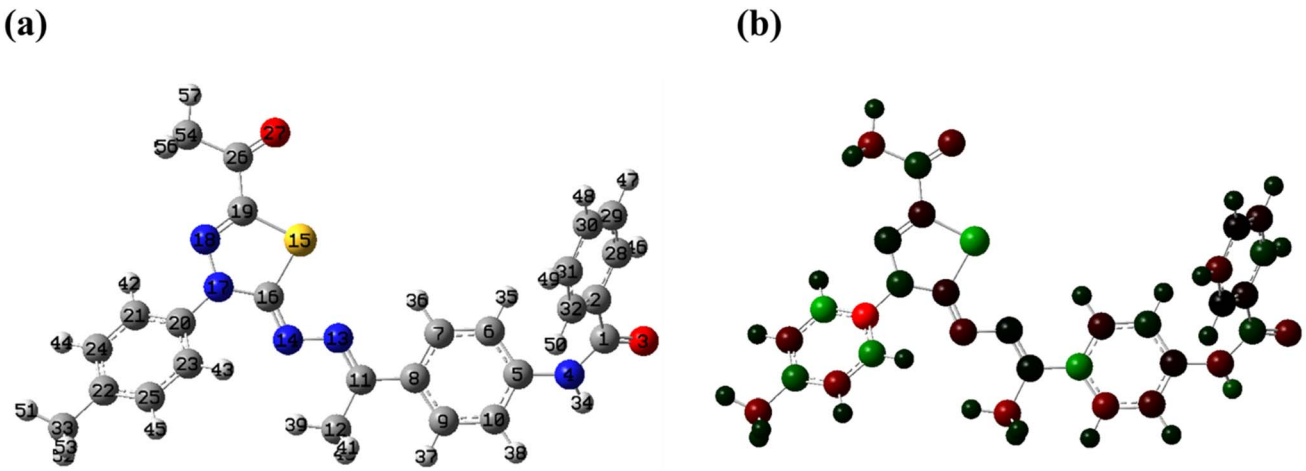

Fig. 6 The entire optimized geometry (a), the distribution of Mullikan atomic charges (b). These results were obtained using B3LYP/6-31+G(d,p).

Table 8 The DFT calculated global reactivity parameters for the molecule under investigation

IP	EA	μ (eV)	χ (eV)	η (eV)	σ (eV)	ω (eV)	Dm (Debye)	TE (eV)	ΔN_{max}	ΔE (eV)
5.684	2.476	−4.080	4.080	1.604	0.624	13.348	7.254	−49717.3	2.544	−13.348

Mulliken charge analysis provides an approximation of the arrangement of electrons for each atom inside a molecule and then it affects the dipole moment, molecular polarizability, and electronic structure. Hence, it can provide an understanding of the chemical behavior of the studied molecule as reactive sites can be identified. The designed candidate, **20b**, in Fig. 6b, shows that sulfur and N17 are acceptors while C21 is the most acceptor site in the molecule. On the other hand, all oxygen and nitrogen (except for N17) are donors because they are negative sites and C20 has the highest negative charge. To get more information about HOMO, LUMO, the total density of states (TDOs), and the quantum theory of atoms in molecule (QTAIM) for compound **20b**, see Fig. S11A–C.†

2.6. *In silico* ADMET analysis

Table 9 presents the *in silico* ADMET results of the new thiadiazole compounds, which offer important information on their possible pharmacokinetic behavior. All compounds except compound **16** have very low levels of blood–brain barrier permeability, which indicates minimal penetration ability into the CNS. Regarding the aqueous solubility, compound **16** showed a low level of solubility whilst the rest of compounds were predicted to have very low levels, indicating that methods to improve their water solubility could be required for efficient delivery. Compound **20b** showed a good amount of absorption, indicating a high probability of systemic availability after treatment. All compounds are anticipated to be non-inhibitors with regard to the CYP2D6 interaction, suggesting a decreased probability of metabolic interactions with medications that are metabolized by this enzyme. Finally yet importantly, all substances, including sorafenib, should bind to plasma proteins >90% of the time. This could have an impact on how the synthesized derivatives are distributed and eliminated.

2.7. *In silico* toxicity analysis

Table 10 reports a comprehensive evaluation of compounds (**16**, **20a**, **20b**, **21a**, **21b**) and the reference compound Sorafenib, with a focus on carcinogenic potency, mutagenicity, and toxicity profiles. In terms of carcinogenic potency (TD_{50}), compound **20b** exhibits a value of 18.94, placing it within the range of the experimental compounds and slightly below Sorafenib (19.23). Notably, all experimental compounds are classified as non-carcinogens, except for sorafenib, which is identified as a single carcinogen.

A crucial aspect of compound evaluation is its mutagenicity, and in this context, compound **20b** is recognized as mutagenic, indicating a potential to induce mutations. Regarding toxicity, all experimental compounds, including **20b**, are categorized as non-toxic, suggesting a favorable safety profile. However, sorafenib is labeled as toxic, indicating a potential for adverse

Table 9 ADMET descriptors of compounds 16, 20a,b and 21a,b

Compound	BBB level	Solubility level	Absorption level	CYP2D6 prediction	PPB prediction
16	2	2	0	False	True
20a	4	1	1		
20b					
21a			2		
21b					
Sorafenib			0		

Table 10 Toxicity study of compounds 16, 20a,b and 21a,b

Compound	Carcinogenicity TD_{50} (Mouse)[a]	Mouse- female FDA	DTP	Rat oral LD_{50}[b]	Rat chronic LOAEL[b]	Dermal irritancy	Ocular irritancy
16	24.8533	Non-carcinogen	Non-toxic	0.663451	0.0754607	Non-irritant	Mild
20a	8.42209			0.703374	0.0790792		
20b	18.9369			0.457358	0.0906188		
21a	17.6022			0.902703	0.0589522		
21b	9.60638			0.896764	0.0336175		
Sorafenib	19.2359	Single-carcinogen	Toxic	0.822583	0.00482816		

[a] Unit: mg kg^{-1} per day. [b] Unit: g kg^{-1}.

effects. Further insights are provided through assessments such as rat oral LD_{50} and chronic LOAEL, where compound **20b** exhibits a lower oral LD_{50} of 0.457358. Additionally, a higher chronic LOAEL of 0.0906188, indicates a safe potential for long-term use. Notably, all compounds, including **20b**, are classified as non-irritants for both skin and ocular irritation, enhancing their safety profile in these regards. In conclusion, compound **20b**'s distinct non-carcinogenic potency and the comparison with sorafenib underscores the general safety. While the current data provide valuable insights, additional *in vivo* assessments and clinical trials are imperative for a comprehensive understanding of the safety and efficacy of compound **20b** for potential therapeutic applications.

3. Conclusion

In conclusion, the comprehensive investigation presented in this paper highlights the promising potential of compound **20b** as a potent anti-proliferative agent. The compound demonstrates significant inhibitory effects on MCF-7 and HepG2 cancer cell lines, with notably low IC_{50} values, suggesting enhanced potency compared to reference compounds. Importantly, the selectivity index values underscore the preferential inhibitory activity of **20b** on cancer cells over normal WI-38 cells, laying the foundation for potential therapeutic applications. The mechanistic insights provided by the study revealed that compound **20b** exerted its effects through multiple ways. The substantial inhibition of VEGFR-2, as evidenced by the low IC_{50} value, suggests a potential disruption of angiogenesis, while alterations in cell cycle distribution and the induction of apoptosis further contribute to its anti-proliferative and cytotoxic effects on cancer cells. Moreover, the upregulation of key apoptotic markers, caspase-8 and caspase-9, as observed in RT-PCR analysis, provides molecular evidence supporting the compound's pro-apoptotic effects. Incorporating *in silico* analyses enhanced our understanding of compound **20b**'s molecular interactions with VEGFR-2, aiding in its rational design and pharmacological profile comprehension. Overall, the findings presented in this study underscore the importance of compound **20b** as a lead compound with multifaceted anti-proliferative properties, encouraging further analyses.

4. Experimental

4.1. Chemistry

4.1.1. General. Detailed information about the apparatus, chemicals, and reagents used in the study can be found in the ESI.† Compounds **2**, **4**, **5a,b**, **7**, **8**, **9**, **12**, and **15** were obtained according to the reported procedures.[49]

4.1.2. General procedure for the synthesis of the final compound 16. Equal amounts of intermediate **15** were subjected to a reaction with hydrazonoyl chloride derivative **5b** in absolute ethanol (20 mL), incorporating triethylamine (1 M). The entire mixture was refluxed for a period of 6 hours. The resulting solid was filtered and washed with hot ethanol, resulting in the production of the final compound **16.**

*4.1.2.1 N-(4-((E)-1-(((Z)-5-Acetyl-3-(p-tolyl)-1,3,4-thiadiazol-2(3H)-ylidene)hydrazono)ethyl) phenyl) acetamide **16**.* Yellow powder (yield, 74%); m.p. = 201–202 °C. Comprehensive data, including detailed information from FT-IR, ^{1}H NMR, ^{13}C NMR and EI-Ms can be found in the ESI.†

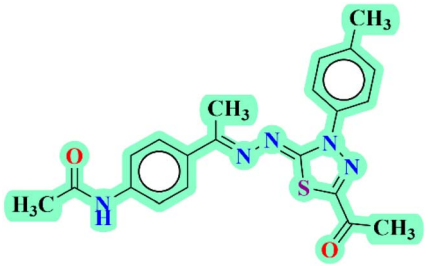

4.1.3. General procedure for the synthesis of derivatives 20a,b and 21a,b. A solution of intermediates **19a,b** (1 M) in ethanol (20 mL) was combined with triethylamine (1 M) and the corresponding hydrazonoyl chlorides **5a,b** and **8** (1 M). The mixtures were heated for a period of 6 hours. The resulting solids were collected and subjected to purification with hexane, resulting in the desired products **20a,b** and **21a,b**, respectively.

*4.1.3.1 N-(4-((E)-1-(((Z)-5-Acetyl-3-(2-chlorophenyl)-1,3,4-thiadiazol-2(3H)-ylidene)hydrazono) ethyl) phenyl)benzamide **20a**.* Pale yellow powder (yield, 70%); m.p. = 190–192 °C. Comprehensive data, including detailed information from FT-IR, ^{1}H NMR, ^{13}C NMR and EI-Ms can be found in the ESI.†

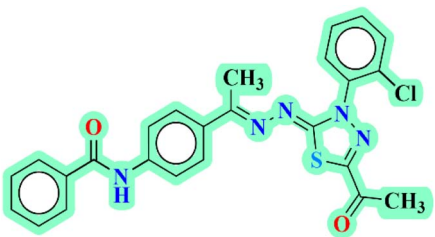

*4.1.3.2 N-(4-((E)-1-(((Z)-5-Acetyl-3-(p-tolyl)-1,3,4-thiadiazol-2(3H)-ylidene)hydrazono) ethyl) phenyl) benzamide **20b**.* Yellow powder (yield, 78%); m.p. = 185–187 °C. Comprehensive data, including detailed information from FT-IR, ^{1}H NMR, ^{13}C NMR and EI-Ms can be found in the ESI.†

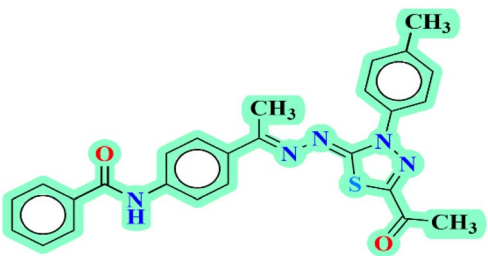

*4.1.3.3 Ethyl (Z)-5-(((E)-1-(4-benzamidophenyl)ethylidene) hydrazono)-4-(3-chlorophenyl)-4,5-dihydro-1,3,4-thiadiazole-2-carboxylate **21a**.* Yellowish white powder (yield, 73%); m.p. = 230–232 °C. Comprehensive data, including detailed information from FT-IR, ^{1}H NMR, ^{13}C NMR and EI-Ms can be found in the ESI.†

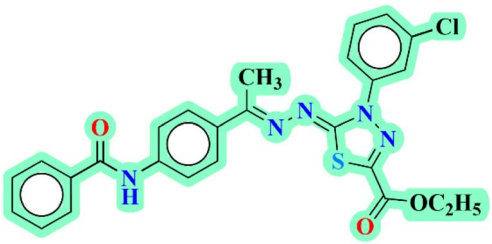

4.1.3.4 Ethyl (Z)-5-(((E)-1-(4-(4-Chlorobenzamido)phenyl) ethylidene)hydrazono)-4-(3-chlorophenyl)-4,5-dihydro-1,3,4-thiadiazole-2-carboxylate ***21b***. Yellow powder (yield, 75%); m.p. = 203–205 °C. Comprehensive data, including detailed information from FT-IR, ^{1}H NMR, ^{13}C NMR and EI-Ms can be found in the ESI.†

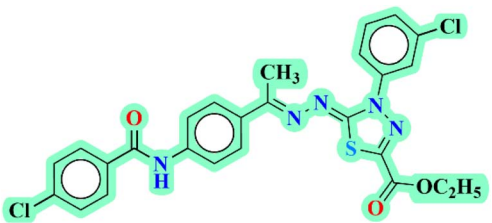

4.2. Biological evaluation

4.2.1. 1. ***In vitro*** **anti-proliferative activity.** MTT assay[50–52] was applied to assess the anti-proliferative activity of the 2,3-dihydro-1,3,4-thiadiazole derived compounds (ESI†).

4.2.2. ***In vitro*** **VEGFR-2 inhibition.** VEGFR-2 ELISA kit[26] was utilized to evaluate the VEGFR-2 inhibitory effect of the 2,3-dihydro-1,3,4-thiadiazole derived compounds (ESI†).

4.2.3. Kinase profiling test. The *in vitro* inhibitory activity of compound **20b** against CDK8, PIK3α, BRAF & EGFR kinases enzyme activities was accomplished using Assay Kits (BPS Bioscience, USA) as shown in ESI.†

4.2.4. Cell cycle and apoptosis analyses. Flow cytometry was used to check the cell cycle and apoptosis behavior of MCF-7 After the application of compound **20b** as shown in ESI.†[53,54]

4.2.5. Assessment of caspase-8 and caspase-9 gene expression. The levels of caspase-8 and caspase-9 in MCF-7 cells treated with compound **20b** were assessed using RT-PCR as described in ESI.†

4.3. *In silico* studies

4.3.1. Docking studies. The synthesized 2,3-dihydro-1,3,4-thiadiazole derived compounds were docked against the VEGFR-2 crystal structure using MOE2019 software[55] (ESI†).

4.3.2. MD simulation studies. GROMACS 2021 (ref. 56) was utilized to study the molecular dynamics (MD) simulations of the VEGFR-2_**20b** complex at 200 nanosecond. Molecular Mechanics Generalized Born Surface Area (MM-GBSA), and Principal Component Analysis (PCA) were performed as shown in ESI.†[57]

4.3.3. DFT analysis. The DFT calculations of compound **20b** were performed using Gaussian09W.01D software as shown in ESI.†[58]

4.3.4. ADMET and toxicity studies. Discovery Studio 4.0 (ref. 59 and 60) was utilized to predict the ADMET and toxicity parameters of the 2,3-dihydro-1,3,4-thiadiazole derived compounds (ESI†).

Data availability

All data regarding the presented work was included in the main manuscript and the ESI.†

Conflicts of interest

The authors verify that they have no conflicts of interest associated with this publication involving any party or among the co-authors.

Acknowledgements

This research was funded by Princess Nourah bint Abdulrahman University Researchers Supporting Project number (PNURSP2024R481), Princess Nourah bint Abdulrahman University, Riyadh, Saudi Arabia. The authors would like to thank AlMaarefa University, Riyadh, Saudi Arabia, for supporting this research.

References

1 W. H. Organization, Global cancer burden growing, amidst mounting need for services, **https://www.who.int/news/item/01-02-2024-global-cancer-burden-growing–amidst-mounting-need-for-services**, accessed 1 February 2024.
2 M. Shibuya, *J. Biochem.*, 2013, **153**, 13–19.
3 L. Claesson-Welsh and M. Welsh, *J. Intern. Med.*, 2013, **273**, 114–127.
4 X. Wang, A. M. Bove, G. Simone and B. Ma, *Front. Cell Dev. Biol.*, 2020, **8**, 599281.
5 K. Cheng, C. F. Liu and G. W. Rao, *Curr. Med. Chem.*, 2021, **28**, 2540–2564.
6 T. A. Farghaly, W. A. Al-Hasani and H. G. Abdulwahab, *Expert Opin. Ther. Pat.*, 2021, **31**, 989–1007.
7 E. B. Elkaeed, R. G. Yousef, H. Elkady, A. B. Mehany, B. A. Alsfouk, D. Z. Husein, I. M. Ibrahim, A. M. Metwaly and I. H. Eissa, *J. Biomol. Struct. Dyn.*, 2023, **41**, 7986–8001.
8 K. Czaja, J. Kujawski, P. Śliwa, R. Kurczab, R. Kujawski, A. Stodolna, A. Myślińska and M. K. Bernard, *Int. J. Mol. Sci.*, 2020, **21**, 4793.
9 J. Versmissen, K. M. Mirabito Colafella, S. L. W. Koolen and A. H. J. Danser, *Cardiovasc. Res.*, 2019, **115**, 904–914.
10 R. M. Hanna, E. A. Lopez, H. Hasnain, U. Selamet, J. Wilson, P. N. Youssef, N. Akladeous, S. Bunnapradist and M. B. Gorin, *Clin. Kidney J.*, 2019, **12**, 92–100.
11 H. Abdel-Qadir, J. L. Ethier, D. S. Lee, P. Thavendiranathan and E. Amir, *Cancer Treat. Rev.*, 2017, **53**, 120–127.
12 X. Li, J. Chai, Z. Wang, L. Lu, Q. Zhao, J. Zhou and F. Ju, *OncoTargets Ther.*, 2018, **11**, 4407–4411.

13 T. M. Sissung, C. J. Peer, N. Korde, S. Mailankody, D. Kazandjian, D. J. Venzon, O. Landgren and W. D. Figg, *Cancer Chemother. Pharmacol.*, 2017, **80**, 217–221.
14 P. Chunarkar-Patil, M. Kaleem, R. Mishra, S. Ray, A. Ahmad, D. Verma, S. Bhayye, R. Dubey, H. N. Singh and S. Kumar, *Biomedicines*, 2024, **12**, 201.
15 K. Balasubramanian, *Reference Module in Biomedical Sciences*, 2021.
16 R. Bozorgpour, S. Sheybanikashani and M. Mohebi, *arXiv*, 2023, preprint, arXiv:2310.19950, 2023.
17 M. S. Taghour, H. Elkady, W. M. Eldehna, N. El-Deeb, A. M. Kenawy, A. E. Abd El-Wahab, E. B. Elkaeed, B. A. Alsfouk, A. M. Metwaly and I. H. Eissa, *J. Biomol. Struct. Dyn.*, 2022, 1–16.
18 E. B. Elkaeed, M. S. Taghour, H. A. Mahdy, W. M. Eldehna, N. M. El-Deeb, A. M. Kenawy, B. A. Alsfouk, M. A. Dahab, A. M. Metwaly and I. H. Eissa, *J. Enzyme Inhib. Med. Chem.*, 2022, **37**, 2191–2205.
19 E. B. Elkaeed, R. G. Yousef, H. Elkady, I. M. Gobaara, B. A. Alsfouk, D. Z. Husein, I. M. Ibrahim, A. M. Metwaly and I. H. Eissa, *Molecules*, 2022, **27**, 4606.
20 R. G. Yousef, A. Elwan, I. M. Gobaara, A. B. Mehany, W. M. Eldehna, S. A. El-Metwally, B. A. Alsfouk, E. B. Elkaeed, A. M. Metwaly and I. H. Eissa, *J. Enzyme Inhib. Med. Chem.*, 2022, **37**, 2206–2222.
21 H. Elkady, A. A. Abuelkhir, M. Rashed, M. S. Taghour, M. A. Dahab, H. A. Mahdy, A. Elwan, H. A. Al-Ghulikah, E. B. Elkaeed, I. M. Ibrahim, D. Z. Husein, A. Metwaly and I. H. Eissa, *Comput. Biol. Chem.*, 2023, **107**, 107958.
22 R. G. Yousef, H. Elkady, E. B. Elkaeed, I. M. Gobaara, H. A. Al-Ghulikah, D. Z. Husein, I. M. Ibrahim, A. M. Metwaly and I. H. Eissa, *Molecules*, 2022, **27**, 7719.
23 I. H. Eissa, R. G. Yousef, H. Elkady, E. B. Elkaeed, A. A. Alsfouk, D. Z. Husein, I. M. Ibrahim, M. A. Elhendawy, M. Godfrey and A. M. Metwaly, *Comput. Biol. Chem.*, 2023, **107**, 107953.
24 H. Elkady, W. E. Elgammal, H. A. Mahdy, S. Zara, S. Carradori, D. Z. Husein, A. A. Alsfouk, I. M. Ibrahim, E. B. Elkaeed and A. M. Metwaly, *Comput. Biol. Chem.*, 2024, 108221.
25 I. H. Eissa, R. G. Yousef, H. Elkady, E. B. Elkaeed, A. A. Alsfouk, D. Z. Husein, I. M. Ibrahim, M. M. Radwan and A. M. Metwaly, *ChemistryOpen*, 2023, **12**, e202300066.
26 H. A. Mahdy, H. Elkady, M. S. Taghour, A. Elwan, M. A. Dahab, M. A. Elkady, E. G. Elsakka, E. B. Elkaeed, B. A. Alsfouk and I. M. Ibrahim, *Future Med. Chem.*, 2023, **15**, 1233–1250.
27 M. A. Dahab, H. A. Mahdy, H. Elkady, M. S. Taghour, A. Elwan, M. A. Elkady, E. G. Elsakka, E. B. Elkaeed, A. A. Alsfouk and I. M. Ibrahim, *J. Biomol. Struct. Dyn.*, 2024, **42**, 4214–4233.
28 E. B. Elkaeed, R. G. Yousef, H. Elkady, A. B. Mehany, B. A. Alsfouk, D. Z. Husein, I. M. Ibrahim, A. M. Metwaly and I. H. Eissa, *J. Biomol. Struct. Dyn.*, 2022, 1–16.
29 E. B. Elkaeed, R. G. Yousef, H. Elkady, I. M. Gobaara, A. A. Alsfouk, D. Z. Husein, I. M. Ibrahim, A. M. Metwaly and I. H. Eissa, *Processes*, 2022, **10**, 1391.
30 M. Szeliga, *Pharmacol. Rep.*, 2020, **72**, 1079–1100.
31 U. A. Atmaram and S. M. Roopan, *Appl. Microbiol. Biotechnol.*, 2022, **106**, 3489–3505.
32 S. Janowska, A. Paneth and M. Wujec, *Molecules*, 2020, **25**, 1–41.
33 A. Ricci, M. Gallorini, D. Del Bufalo, A. Cataldi, I. D'Agostino, S. Carradori and S. Zara, *Molecules*, 2022, **27**, 1–20.
34 L. Huang, Z. Huang, Z. Bai, R. Xie, L. Sun and K. Lin, *Future Med. Chem.*, 2012, **4**, 1839–1852.
35 W. Tang, Z. Chen, W. Zhang, Y. Cheng, B. Zhang, F. Wu, Q. Wang, S. Wang, D. Rong and F. Reiter, *Signal Transduction Targeted Ther.*, 2020, **5**, 87.
36 L. J. Scott, *Drugs*, 2015, **75**, 553–560.
37 L. Q. Chow and S. G. Eckhardt, *J. Clin. Oncol.*, 2007, **25**, 884–896.
38 C. R. Prakash, P. Theivendren and S. Raja, *Pharmacol. Pharm.*, 2012, **3**, 62–71.
39 K. Lee, K.-W. Jeong, Y. Lee, J. Y. Song, M. S. Kim, G. S. Lee and Y. Kim, *Eur. J. Med. Chem.*, 2010, **45**, 5420–5427.
40 V. A. Machado, D. Peixoto, R. Costa, H. J. Froufe, R. C. Calhelha, R. M. Abreu, I. C. Ferreira, R. Soares and M.-J. R. Queiroz, *Bioorg. Med. Chem.*, 2015, **23**, 6497–6509.
41 Z. Wang, N. Wang, S. Han, D. Wang, S. Mo, L. Yu, H. Huang, K. Tsui, J. Shen and J. Chen, *PLoS One*, 2013, **8**, e68566.
42 J. Dietrich, C. Hulme and L. H. Hurley, *Bioorg. Med. Chem.*, 2010, **18**, 5738–5748.
43 Q.-Q. Xie, H.-Z. Xie, J.-X. Ren, L.-L. Li and S.-Y. Yang, *J. Mol. Graphics Modell.*, 2009, **27**, 751–758.
44 R. N. Eskander and K. S. Tewari, *Gynecol. Oncol.*, 2014, **132**, 496–505.
45 R. Verhé, L. De Buyck, N. De Kimpe, A. De Rooze and N. Schamp, *Bull. Soc. Chim. Belg.*, 1978, **87**, 143–152.
46 S. R. Donohue, R. F. Dannals, C. Halldin and V. W. Pike, *J. Med. Chem.*, 2011, **54**, 2961–2970.
47 L. Yurttaş, Y. Özkay, G. Akalın-Çiftçi and Ş. Ulusoylar-Yıldırım, *J. Enzyme Inhib. Med. Chem.*, 2014, **29**, 175–184.
48 D. L. Klayman, J. F. Bartosevich, T. S. Griffin, C. J. Mason and J. P. Scovill, *J. Med. Chem.*, 1979, **22**, 855–862.
49 W. E. Elgammal, H. Elkady, H. A. Mahdy, D. Z. Husein, A. A. Alsfouk, B. A. Alsfouk, I. M. Ibrahim, E. B. Elkaeed, A. M. Metwaly and I. H. Eissa, *RSC Adv.*, 2023, **13**, 35853–35876.
50 T. Mosmann, *J. Immunol. Methods*, 1983, **65**, 55–63.
51 F. Denizot and R. Lang, *J. Immunol. Methods*, 1986, **89**, 271–277.
52 M. Thabrew, R. D. Hughes and I. G. Mcfarlane, *J. Pharm. Pharmacol.*, 1997, **49**, 1132–1135.
53 A. R. Kotb, A. E. Abdallah, H. Elkady, I. H. Eissa, M. S. Taghour, D. A. Bakhotmah, T. M. Abdelghany and M. A. El-Zahabi, *RSC Adv.*, 2023, **13**, 10488–10502.
54 S. A. El-Metwally, H. Elkady, M. Hagras, E. B. Elkaeed, B. A. Alsfouk, A. S. Doghish, I. M. Ibrahim, M. S. Taghour, D. Z. Husein and A. M. Metwaly, *Future Med. Chem.*, 2023, **15**, 2065–2086.
55 Y. M. Suleimen, R. A. Jose, G. K. Mamytbekova, R. N. Suleimen, M. Y. Ishmuratova, W. Dehaen,

B. A. Alsfouk, E. B. Elkaeed, I. H. Eissa and A. M. Metwaly, *Plants*, 2022, **11**, 2072.
56 M. J. Abraham, T. Murtola, R. Schulz, S. Páll, J. C. Smith, B. Hess and E. Lindahl, *SoftwareX*, 2015, **1**, 19–25.
57 A. Amadei, A. B. Linssen and H. J. Berendsen, *Proteins: Struct., Funct., Bioinf.*, 1993, **17**, 412–425.
58 D. Z. Husein, R. Hassanien and M. Khamis, *Asian J. Chem.*, 2021, **11**, 27027–27041.
59 D. Studio, *Accelrys*, 2008, **420**, 1–2.
60 A. M. Metwaly, E. B. Elkaeed, B. A. Alsfouk, A. M. Saleh, A. E. Mostafa and I. H. Eissa, *Plants*, 2022, **11**(14), 1–19.